10
Improved constraint of magnetisation direction from UAV surveys of under-sampled aeromagnetic anomalies

C.A. Foss, M. Takáč and G. Kletetschka

ABSTRACT

Aeromagnetic surveys are a rapid and relatively cheap method of remote sensing to map the distribution of sub-surface magnetisations. They cover large areas but at a line spacing that is a compromise between resolution of the data and cost. Sampling sufficiency of aeromagnetic data is particularly a problem for investigation of small, shallow magnetisations. We investigate limitations in mapping both the spatial distribution of magnetisation and its direction from sparsely sampled data and illustrate this analysis using two anomalies measured in aa aeromagnetic survey flown at 250 m line spacing over parts of New South Wales and the Australian Capital Territory. The anomalies are due to adjacent shallow remanence-dominated magnetisations. We show that from the aeromagnetic data the direction of magnetisation is weakly constrained for the larger body and is even more uncertain for the smaller body. We flew two UAV surveys at 58 and 35 m elevation and 20 m line spacing. From the UAV surveys we recovered more reliable estimates of source magnetisation direction for both bodies. An effective survey strategy is to fly aeromagnetic surveys at line spacings close enough to confidently detect anomalies of interest and then fly UAV surveys over selected areas where estimates of source magnetisation need to be upgraded.

10.1 ESTIMATION OF MAGNETISATION DIRECTION FROM MAGNETIC FIELD ANALYSIS OF COMPACT SOURCES

Helbig (1963) established that the direction of magnetisation for a dipole of known location can be uniquely derived from analysis of its external magnetic field, and Zietz and Andreasen (1967) showed that in a steep inclination northern hemisphere geomagnetic field the declination of magnetisation of a compact source can be estimated from the azimuth of its total magnetic intensity (TMI) peak to trough vector and the inclination of magnetisation can be estimated from the peak to trough (P:T) amplitude ratio. Figure 10.1 shows an induced magnetisation anomaly over a dipole in a geomagnetic field of inclination −60° (Fig. 10.1A) and anomalies due to a 30° clockwise horizontal rotation of magnetisation direction (Fig. 10.1B), 30° shallowing (Fig. 10.1C) and 30° steepening (Fig. 10.1D). In this southern hemisphere geomagnetic field, declination of magnetisation is indicated by the trough to peak azimuth as opposed to the peak to trough azimuth in the northern hemisphere. The TMI anomaly of the northerly directed induced magnetisation in Fig. 10.1A has a trough to peak azimuth of 0° and a P:T ratio of 5.54. The anomaly for the 30° horizontal clockwise rotation of magnetisation (Fig. 10.1B) causes a 31° rotation of the trough to peak azimuth

and only a minor adjustment of the P:T ratio to 8.1:0. The 30° shallowing of magnetisation (Fig. 10.1C) does not rotate the trough to peak azimuth but reduces the P:T ratio to 2.10, and the 30° steepening of magnetisation direction (Fig. 10.1D) also leaves the trough to peak azimuth unrotated but increases the P:T ratio to 12.93. These relationships are consistent with the Zietz and Andreasen (1967) observations and predictions for anomalies in a steep geomagnetic field.

For the well-defined anomalies shown in Fig. 10.1 the directions of magnetisation can be reliably estimated from their anomaly patterns. However, if the anomalies are only sampled on one or two flightlines there is insufficient information to reliably map those patterns. For instance, if the anomaly is only measured on a single central east–west profile the anomaly trough is not sampled and neither the trough to peak azimuth or peak to trough ratio can be determined.

Figure 10.2 shows flightline plans for a 400 m line-spaced survey superimposed on an image of the TMI field of a vertical circular cylinder of radius 100 m, depth extent 150 m and depth to top 100 m below the computed field elevation. The magnetisation has an intensity of 5 Amp/metre and is parallel to the local geomagnetic field of inclination −60°, declination 000°. The flightlines in Fig. 10.2A are centred over the magnetisation and the flightlines in Fig. 10.2B are off-centred by 200 m (50% of the line spacing). Figure 10.3 shows stacked profiles of TMI measured on these flightlines. The top row (Figs 10.3A and 10.3C) shows stacked profiles for body-centred surveys along north–south and east–west flightlines respectively. In each case a single profile records high amplitudes of the main anomaly peak with much lower amplitudes on the adjacent lines displaced 400 m from the anomaly peak.

The bottom row of Fig. 10.3 (Figs 10.3B and 10.3D) shows stacked profiles for the off-centred surveys along north–south and east–west profiles respectively. For both flightline orientations the anomaly is predominantly expressed on two adjacent profiles. For the north–south profiles (Fig. 10.3B) the two profiles are identical and of significantly lower amplitude than the missing central profile through the anomaly peak (Fig. 10.3A). TMI variations on the east–west profiles (Fig. 10.3D) are of opposite polarities. The substantial differences between adjacent profiles in Figs 10.3A and 10.3B and in Figs 10.3C and 10.3D reveal that for either profile orientation, definition of the magnetic field would benefit considerably from closer line-spaced coverage.

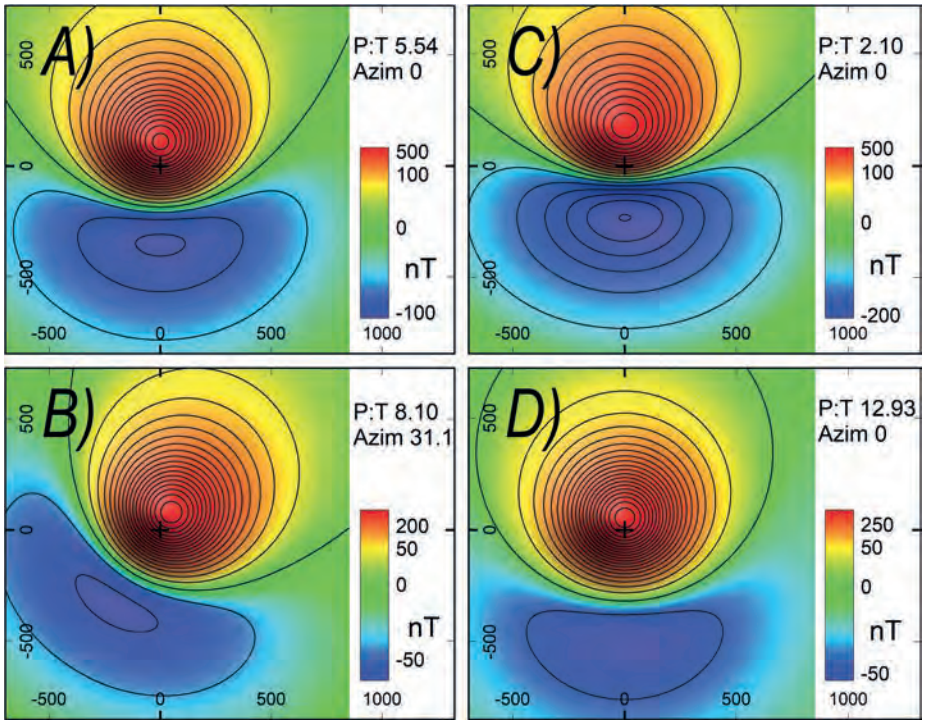

Fig. 10.1. TMI anomalies in a geomagnetic field of declination 0°, Inclination −60° for dipole magnetisations with centre at 400 m depth and magnetisation directions: A) Dec 0° Inc. −60°, B) Dec 30° Inc. −60°, C) Dec 0° Inc. −30°, D) Dec 0°, Inc. −90°.

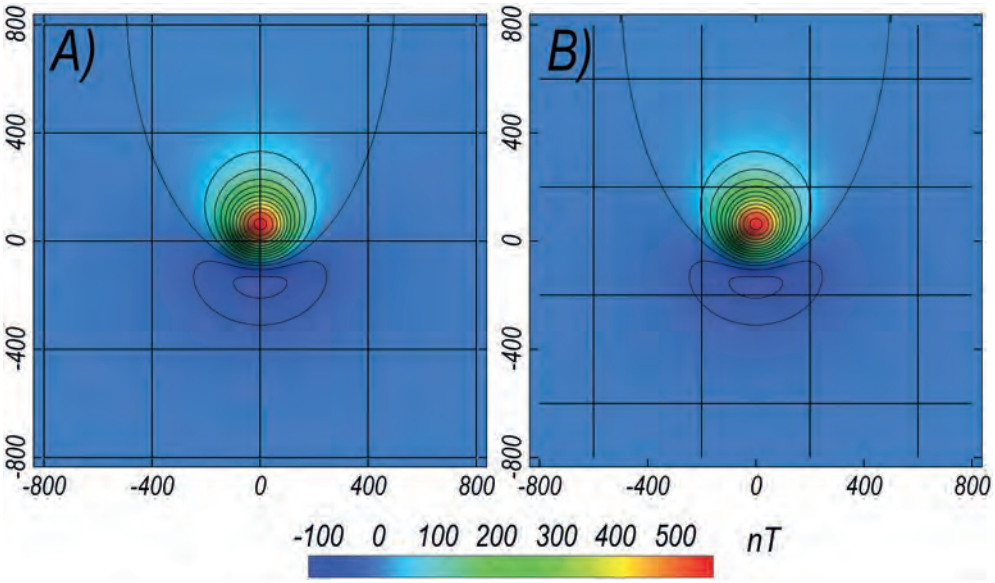

Fig. 10.2. TMI anomalies due to a vertical cylinder of 100 m radius, depth to top 100 m and depth extent 150 m in a geomagnetic field of declination 0°, Inclination −60° with overlays of flightline plans at 400 m spacing: A) centred on the body and B) off-centred.

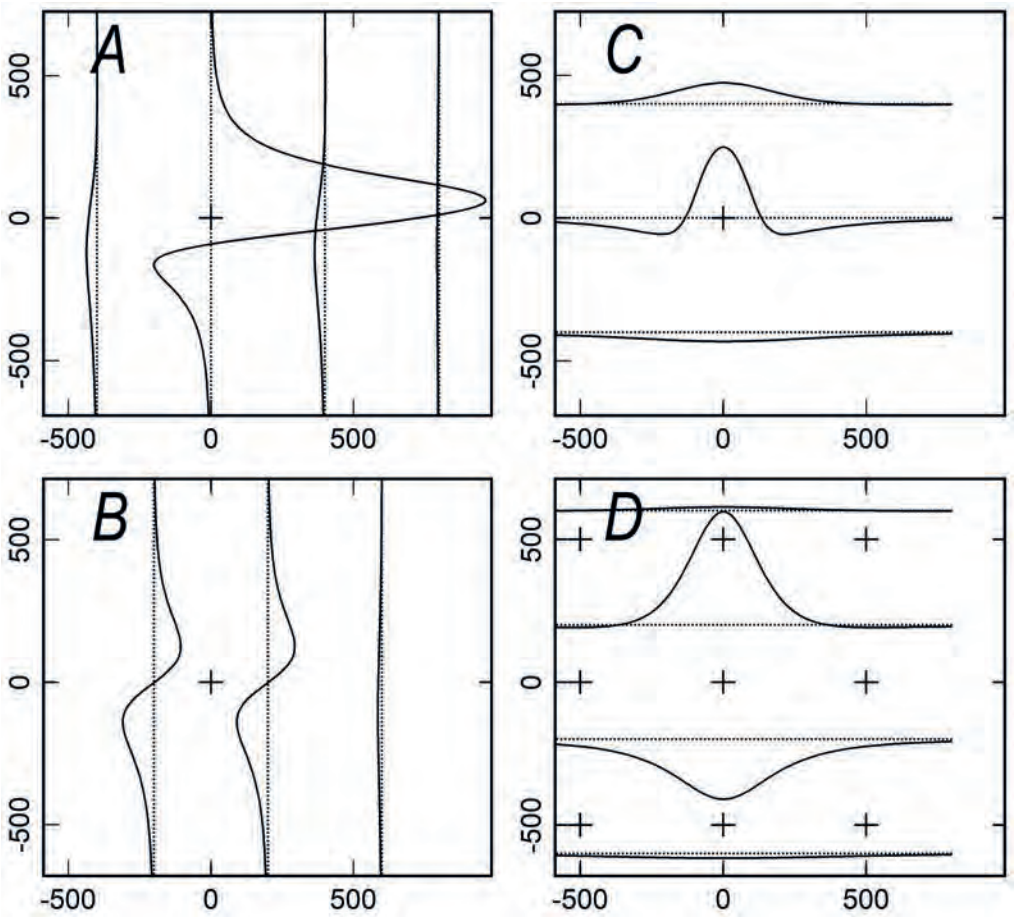

Fig. 10.3. Stacked profiles of TMI for the flightlines shown in Fig. 10.2: A) on-centred N–S lines, B) off-centred N–S lines, C) on-centred E–W lines, D) off-centred E–W lines.

The pattern of TMI variation along each profile in Fig. 10.3 is consistent with the computed TMI images of Fig. 10.2 but the images of Fig. 10.2 cannot be generated from the limited sampling of either 400 m spaced profile set. Anomaly images generated by gridding of each of the four individual 400 m profile sets are shown in Fig. 10.4. All four images are quite different, revealing both the insufficiency of the individual profile sets in sampling the magnetic field and also the substantial influence of flightline orientation. The images from gridding the body-centred profile sets (Figs 10.4A and 10.4C) both peak close to the centre of magnetisation and have peak amplitudes close to the input anomaly peak amplitude. Neither grid image in Figs 10.4A or 10.4C reliably reveals the declination of magnetisation. For the grid in Fig. 10.4A the trough to peak azimuth is constrained by the north–south profile orientation and the grid of Fig. 10.4C is derived from data that do not sample the anomaly trough at all (see Fig. 10.2A). As a consequence, neither declination or inclination of the magnetisation can be reliably determined from these grids.

The grid images of Figs 10.4B and 10.4D are derived from the off-centred profile sets that do not sample the sharp curvatures and high amplitudes at the centre of the anomaly. These grids are even less satisfactory representations of the true field than are the grids from the body-centred profile sets and their lack of sharp curvature suggests that the magnetisation is deeper than it really is.

Total gradient (TG) transforms (Roest and Pilkington 1993; Medeiros and Silva 1995; Wijns *et al*. 2005; Li 2006) and normalised source strength (NSS) transforms (Beiki *et al.* 2012) can be applied to TMI grids to highlight the centre of a magnetisation with reduced dependence on magnetisation direction. However, these gradient dependant enhancements of data are more demanding of sampling sufficiency (Reid 1980). TG transforms of the four TMI grids in Fig. 10.4 are imaged in Fig. 10.5. For the anomaly detected on the body-centred surveys (Figs 10.5A and 10.5C) the TG anomalies are point anomalies centred on the highest sampled TMI value and with minor elongation in the along-line direction (north–south in Fig. 10.5A and east–west in Fig. 10.5C). For the off-centred surveys (Figs 10.5B and 10.5D) the TG peaks are also centred on the extreme sampled TMI values. Gradient enhancement images with peaks centred only on the flightlines is one indication that a magnetic field is most likely under-sampled by the available measurements. For the off-centred north–south flightline survey

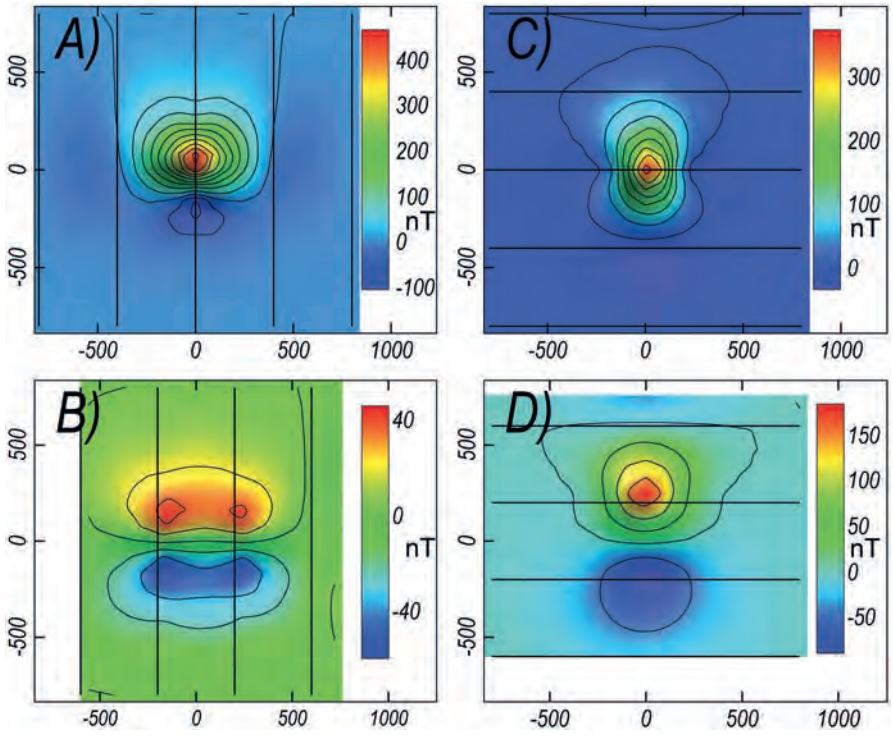

Fig. 10.4. TMI images from gridding of flightline data at 400 m spacing over a vertical cylinder of radius 100 m and depth to top 100 m: A) on-centred N–S lines, B) off-centred N–S lines, C) on-centred E–W lines, D) off-centred E–W lines. Magnetic field and magnetisation directions are both declination 0°, inclination −60°.

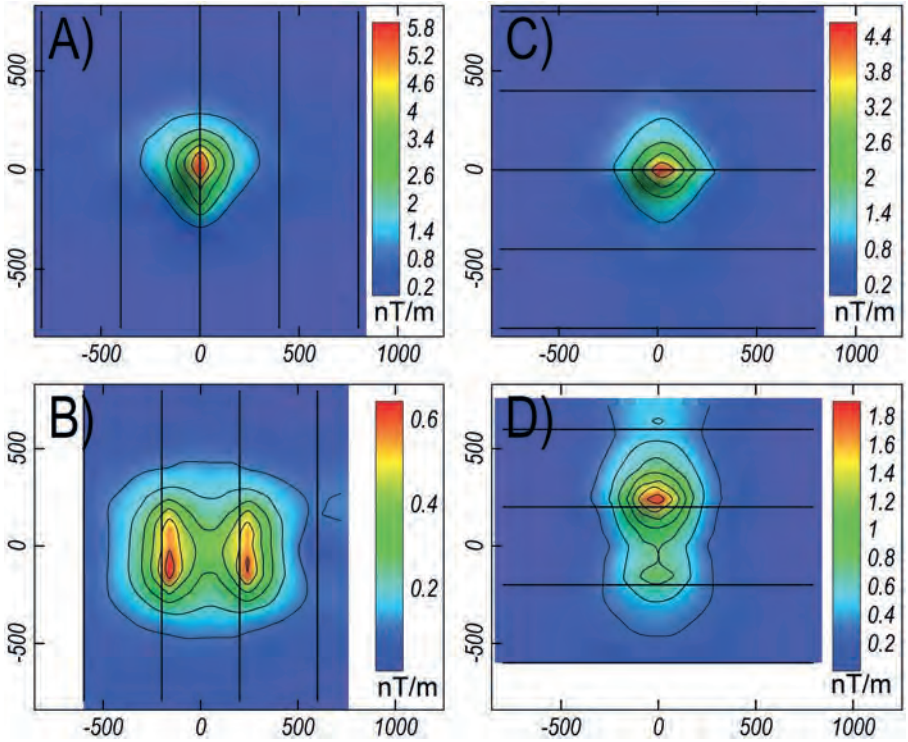

Fig. 10.5. Total gradient (TG) transforms of the grids in Fig. 10.4.

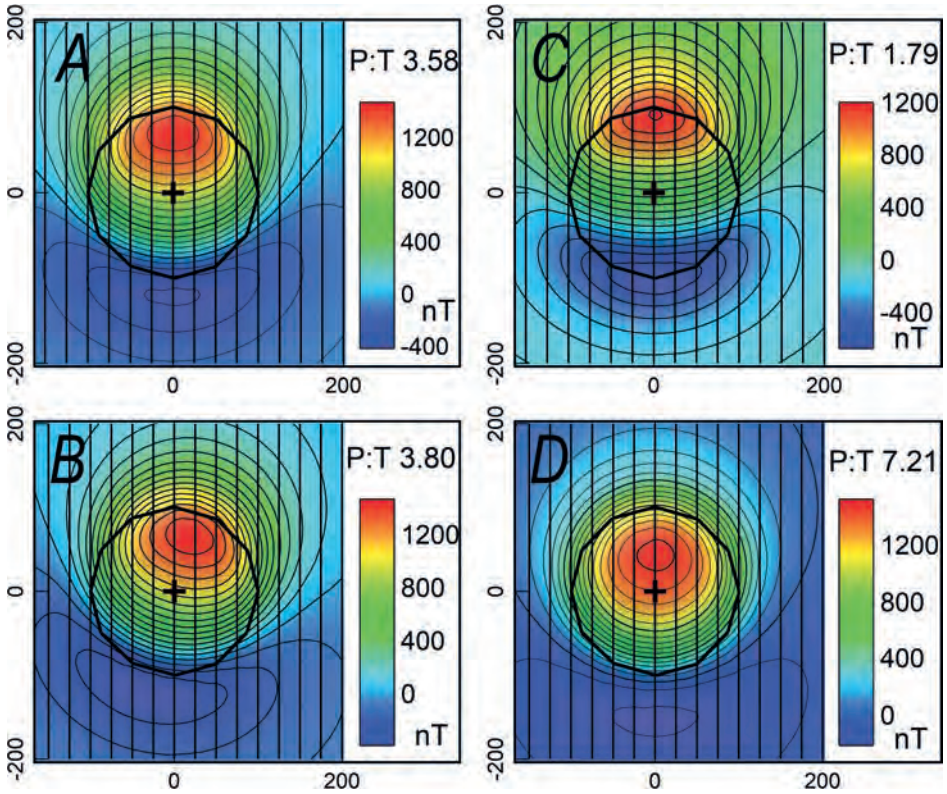

Fig. 10.6. TMI images over the same vertical pipe as for the images of Figs 10.2 to 10.5 but at a reduced elevation of 40 m above the pipe and reduced line spacing of 25 m. Magnetisation directions: A) Dec 0° Inc. −60°, B) Dec 30° Inc. −60°, C) Dec 0° Inc. −30°, D) Dec 0°, Inc. −90°. The geomagnetic inclination is −60°.

(Fig. 10.5C) the grid peaks identically and with strong north–south trend on the two flightlines offset to either side of the anomaly. TG transform of the off-centred east–west flightline survey data also produces two peaks, but in this case the southerly TG peak due to the TMI anomaly trough is less prominent than the northerly TG peak due to the TMI anomaly peak. NSS transforms of the data produce very similar results to the TG transforms and neither transform provides advantage in imaging this under-sampled data other than by highlighting insufficiency of the sampling.

Figure 10.6 shows images of the TMI field computed from the same vertical axis, circular section magnetisation as for Figs 10.2 to 10.5 but in this case with the field computed on more closely spaced lines at 25 m spacing and at the lower elevation of 40 m above the top of the magnetisation. Despite the increased spatial resolution demands of mapping a sharper gradient field at a lower elevation, the substantial reduction in line spacing from 400 m to 25 m provides a far more sufficient sampling of the magnetic field. Figures 10.6A and 10.6B clearly reveal the difference in trough to peak orientation distinctive of the 30° difference in declination of those magnetisations and from both images it is feasible to recover reliable estimates of declination. Figures 10.6B, 10.6A and 10.6C show the change in magnetic fields due to progressive shallowing of a northerly directed magnetisation with inclinations of –90°, –60° and –30° respectively. Consistent with predicted behaviour, the P:T ratio for these three inclinations reduces with reduced steepness of inclination with values of 7.2, 3.6 and 1.8. These values are similar to those for the dipole magnetisations imaged in Figs 10.1D, 10.1A and 10.1C that have values of 12.9, 5.5 and 2.1. The improvements in mapping the magnetic field and recovering source magnetisation information from the lower level, more closely spaced data illustrate the advantage we should expect in flying an unmanned aerial vehicle (UAV) survey to further investigate an anomaly discovered but incompletely specified on a regional aeromagnetic survey.

10.2 THE AEROMAGNETIC ANOMALIES NEAR JINDABYNE, NSW

Figure 10.7 shows the location of an aeromagnetic anomaly south-west of Canberra which we investigated with low elevation and closely spaced UAV surveys. The regional aeromagnetic survey covers part of the Lachlan Orogen (Foster and Gray 2000) and was flown in 2010 by

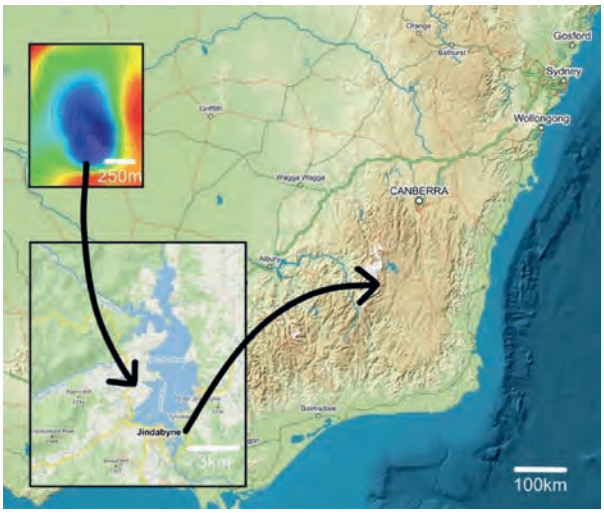

Fig. 10.7. Location map of the main negative aeromagnetic anomaly measured over the west bank of Lake Jindabyne south-west of Canberra.

Fugro Airborne Surveys for the Geological Survey of New South Wales using a fixed-wing Pacific Air Cresco on east–west flight lines at a nominal terrain clearance of 60 m and 250 m spacing. The magnetic field measurements were made with a Scintrex CS-2 magnetometer at a 10 Hz sampling interval giving a point spacing of ~8 m. The aeromagnetic survey is number P1218 in the Geoscience Australia GADDS directory and data can be downloaded from: https://portal.ga.gov.au/persona/gadds.

Figure 10.8 shows a TMI image of a part of the Lachlan aeromagnetic survey. The inset highlights a prominent negative anomaly and a weaker negative anomaly to the south of it. The north–south extent of the main anomaly is 500 m with an amplitude of –470 nT. The smaller anomaly is defined on only one flightline with an amplitude of –190 nT.

As shown by the section of the geological map by Lewis and Glen (1995) in Fig. 10.9, the anomaly location to the west of Lake Jindabyne is mapped as part of the Jindabyne Suite I type Kosciusko Batholith with a main reported lithology of hornblende and biotite bearing tonalite (Lewis *et al*. 1994). However, the small, shallow, reversely magnetised sources of the magnetic anomalies are likely to be small plugs of Cainozoic Monaro Province Volcanics. These feeder pipes and minor relicts of basalt flows poorly outcrop but are reported across an area 100 km north–south by 35 km east–west (see fig. 10.35 of Lewis *et al*. 1994) including known occurrences that correlate with similar magnetic anomalies. The geological mapping was

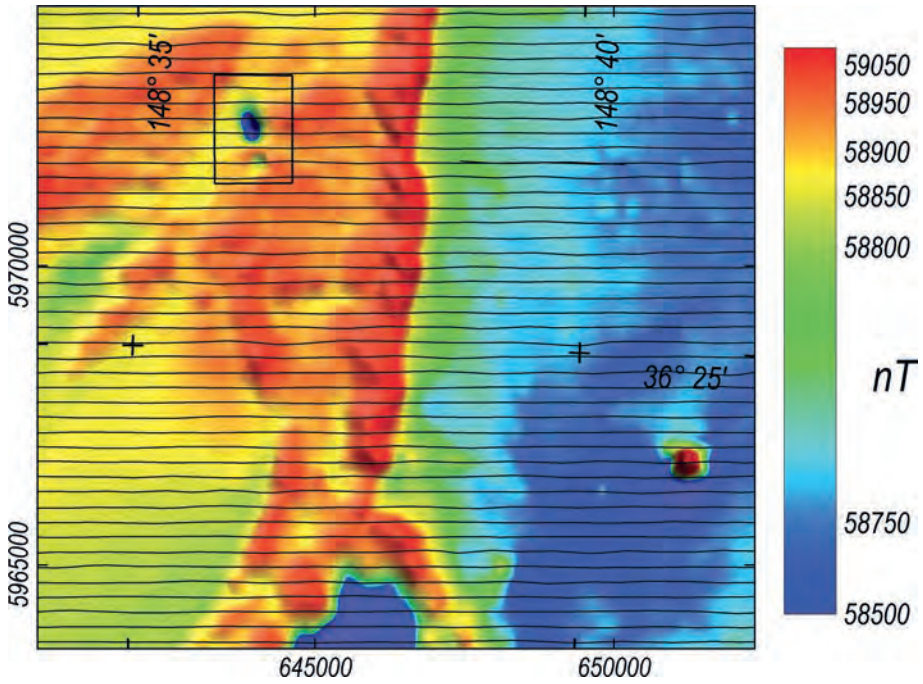

Fig. 10.8. TMI image of a section of the P1218 regional aeromagnetic survey. The inset shows the negative Lake Jindabyne anomaly.

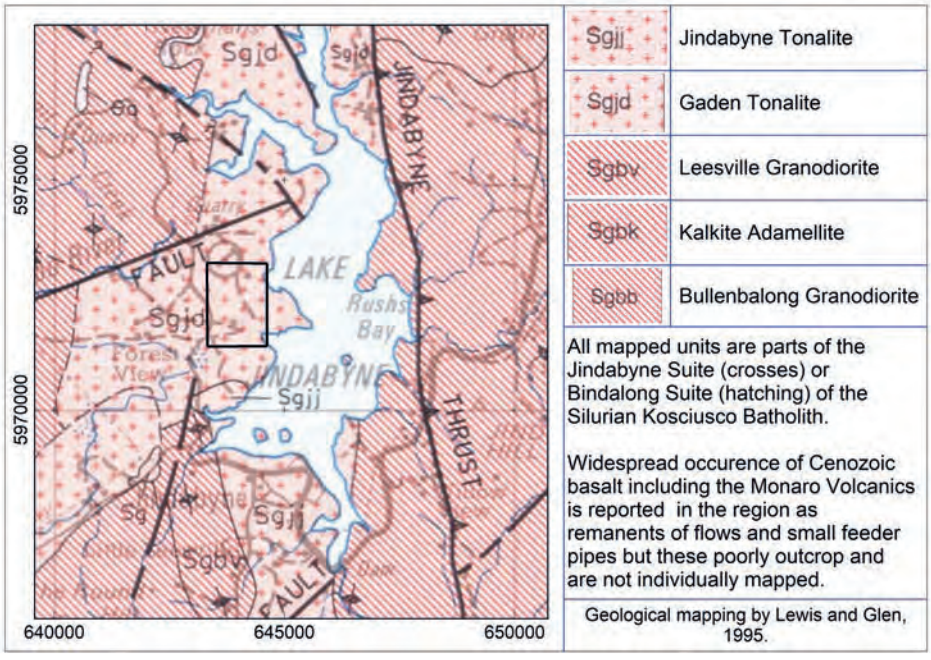

Fig. 10.9. Section of the Bega-Malcoota 1:250,000 geological map (Lewis and Glen 1995).

undertaken before the aeromagnetic survey was flown and had the aeromagnetic and radiometric data been available at the time of the geological mapping these data would most likely have been used to supplement the surface mapping of these strongly magnetic but mostly recessive or covered units.

Figure 10.10A shows TMI variation across the study area (shown as an inset in Figs 10.8 and 10.9). The main anomaly is defined on two east–west flight lines. The line immediately to the south of those is beyond the main anomaly and the line to the north defines the flank of the anomaly but with an amplitude of only

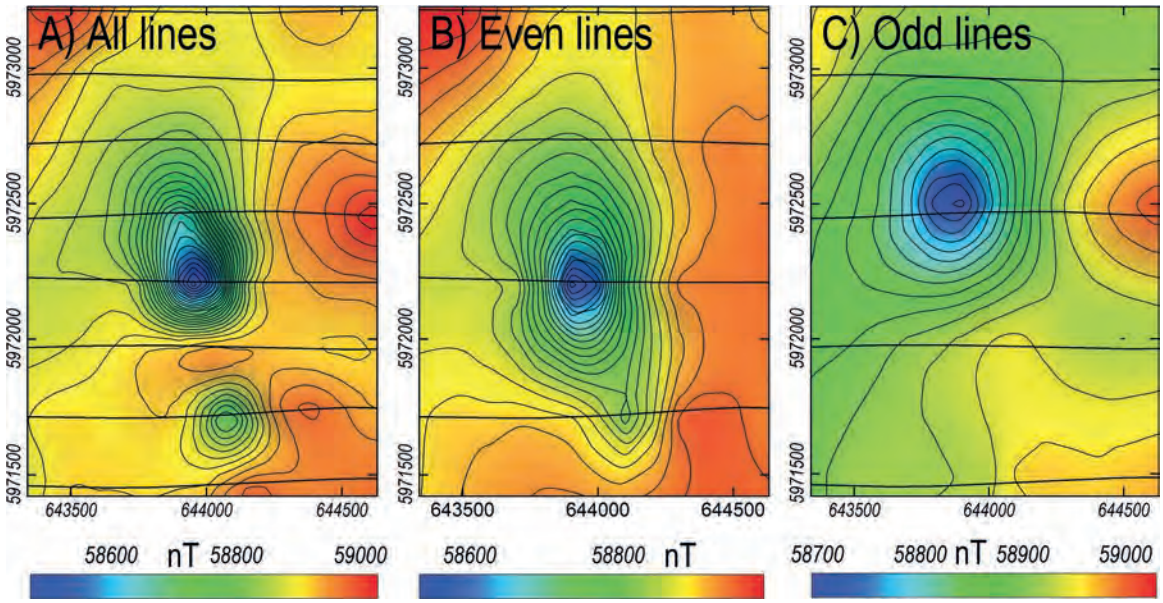

Fig. 10.10. Aeromagnetic survey TMI images of: A) all lines (250 m spacing), B) even lines, C) odd lines.

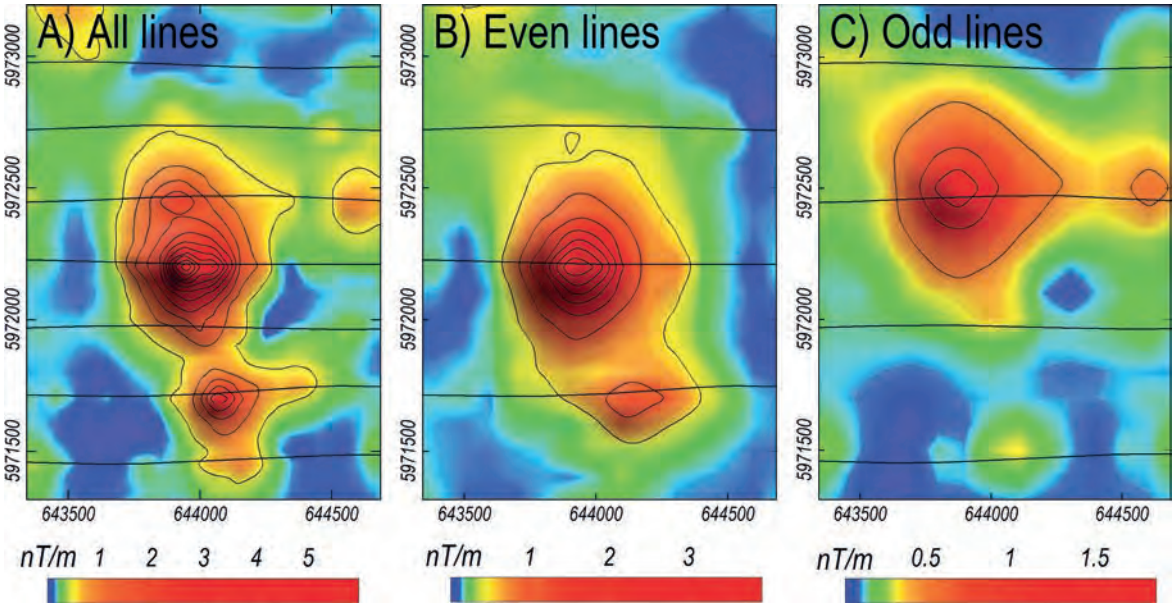

Fig. 10.11. Total gradient (TG) transforms of the TMI grids in Fig. 10.10.

–15 nT (3% of the anomaly trough). The southern anomaly is defined on only a single line. Figures 10.10B and 10.10C show quite different images from gridding of alternate flightlines at 500 m spacing. The image from the even-numbered flightlines in Fig. 10.10B includes the only flightline through the southern anomaly but excludes the flightline between the anomalies, so the gridding joins the two anomalies. The image from the odd-numbered flightlines in Fig. 10.10C excludes the flightline on which the southern anomaly is defined as well as the key flightline through the centre of the main anomaly, producing a mapping of a single anomaly of lower amplitude, displaced to the north. The insufficiency of these 500 m line-spaced data selections revealed by the abrupt differences between them suggests that the 250 m line-spaced survey is itself undersampled. This insufficiency is further highlighted in Fig. 10.11 that shows total gradient of TMI computed from the survey data (Fig. 10.11A) and from the two alternate-line subsets (Figs 10.11B and 10.11C).

10.2.1 Modelling of the aeromagnetic data

Two inversions of the aeromagnetic survey data were performed, one using a model of two ellipsoids and the other using a model of two elliptic-section pipes. Both inversions allowed a free direction of magnetisation and both models match the input data equally well with no clear justification to favour either model over the other. Sections along the two key flight lines through the main and southern anomalies are shown in Fig. 10.12. The pipe models with horizontal top surfaces and abrupt edges are suitable for estimation of depth to the top of magnetisation but the under-sampled data makes depth estimation unreliable. The two inversions co-locate the magnetisations (see Figs 10.12 and 10.13) and estimate very similar magnetisation directions (see Table 10.1). Figure 10.14 shows measured TMI and TMI forward computed from the elliptic pipes inversion model. The under-sampling of the aeromagnetic anomalies makes it easier to find a close fit to the input data by inversion. However, the inversion models are of low reliability because the sample of data they are derived from is inadequate.

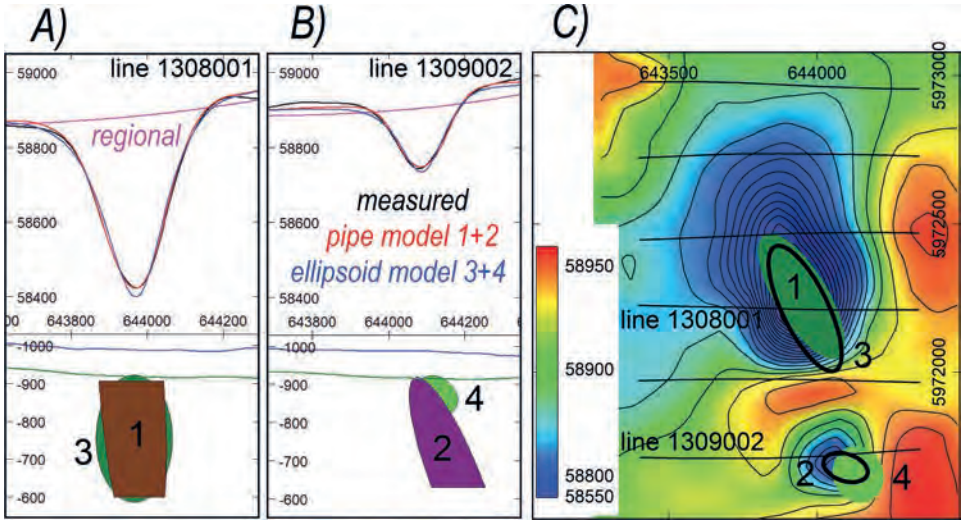

Fig. 10.12. Key aeromagnetic flightline cross-sections through the inversion models and image of model-computed TMI for the elliptic pipe models 1 and 2. The ellipsoid models 3 and 4 produce an almost identical field.

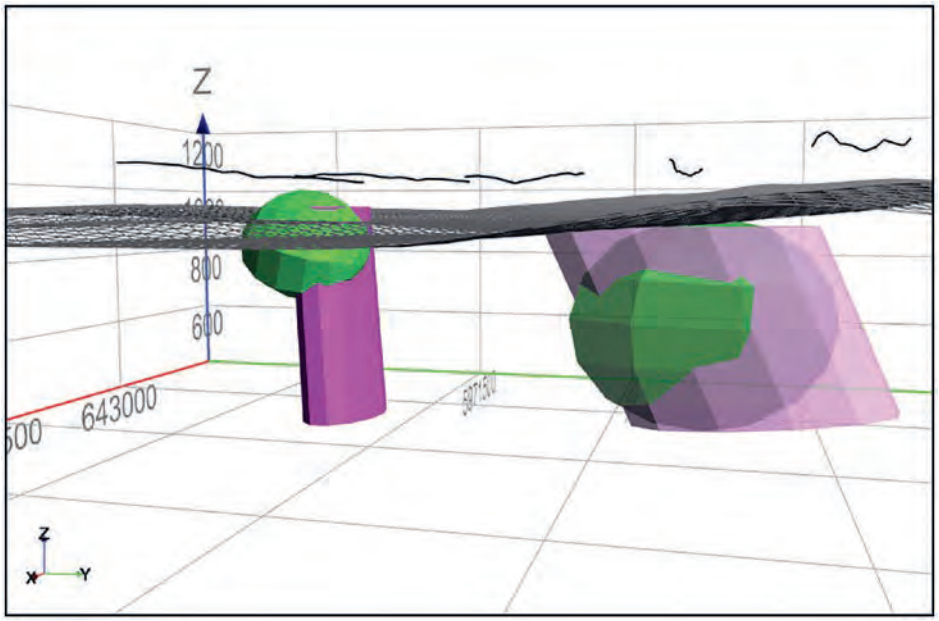

Fig. 10.13. Perspective view of the inversion models shown in Fig. 10.12.

Table 10.1. Inversion model magnetisation details.

Survey	Anomaly	ARAD	Geometry	J_int A/m	J_dec	J_inc	Volume m^3	Moment $A.m^2$
P1218	Main	309	Ellipsoid	2.11	98	60	29.3×10^6	62×10^6
P1218	Main	309	Elliptic pipe	2.28	80	61	36.3×10^6	83×10^6
P1218	Main	309	Frustum	2.33	82	55	37.2×10^6	87×10^6
P1218	**Main**	**Mean(3)**		**2.24**	**86**	**59**	**34.3×10^6**	**77×10^6**
Drone_980	Main	314_377	Ellipsoid	14.7	55	59	1.69×10^6	25×10^6
Drone_980	Main	314_378	Elliptic pipe	6.42	57	68	4.09×10^6	26×10^6
Drone_980	Main	314_379	Frustum	6.76	84	70	4.37×10^6	30×10^6
Drone_980	**Main**	**Mean(3)**		**9.29**	**64**	**66**	**3.38×10^6**	**27×10^6**
Drone_980	South	315_380	Ellipsoid	4.05	39	56	0.62×10^6	2.5×10^6
Drone_980	South	315_381	Elliptic pipe	3.21	51	55	1.28×10^6	4.1×10^6
Drone_980	South	315_382	Frustum	2.15	50	55	1.94×10^6	4.2×10^6
Drone_980	**South**	**Mean(3)**		**3.14**	**47**	**55**	**1.28×10^6**	**3.6×10^6**
Drone_950	South	316	Ellipsoid	5.79	63	69	1.87×10^3	11×10^3
Drone_950	South	316	Elliptic pipe	4.92	55	60	2.33×10^3	11×10^3
Drone_950	South	316	Frustum	4.92	55	65	2.48×10^3	12×10^3
Drone_950	**South**	**Mean(3)**		**5.21**	**57**	**65**	**2.23×10^3**	**11×10^3**
	LARGE	**MEAN(6)**		**5.8**	**76**	**63**	**18.9×10^6**	**52×10^6**
	SMALL	**MEAN(6)**		**3.9**	**51**	**60**	**1.9×10^3**	**7.6×10^3**

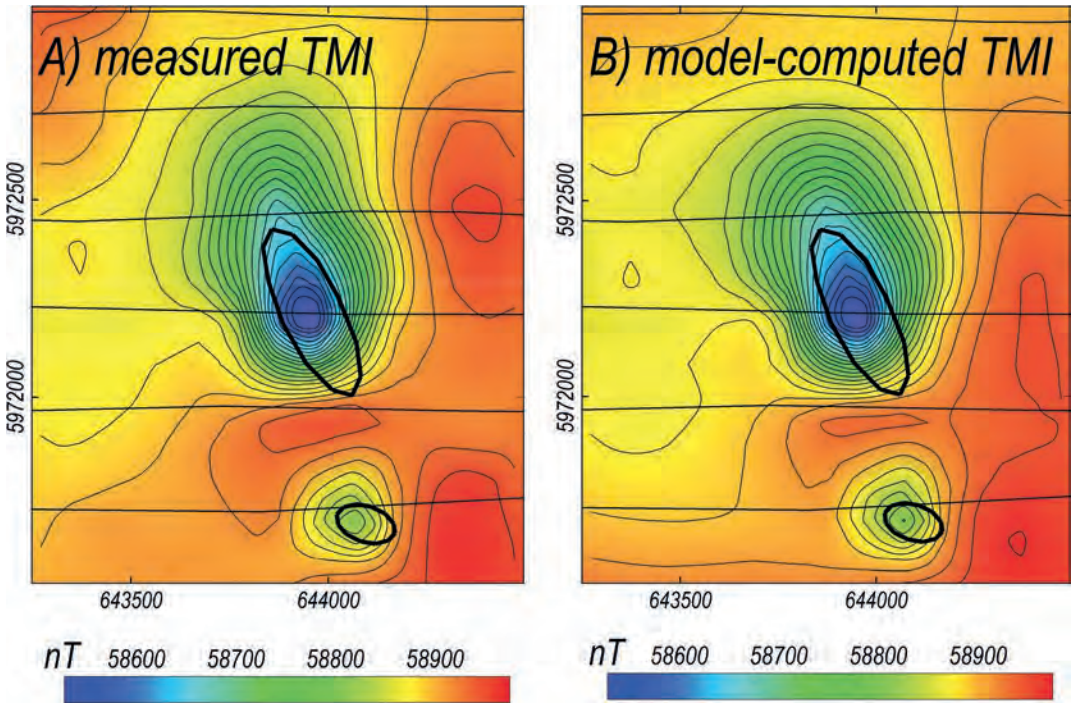

Fig. 10.14. A) measured TMI from the P1218 aeromagnetic survey, and B) TMI forward computed from the elliptic pipe inversion model.

10.3 THE UAV SURVEY OVER THE JINDABYNE AEROMAGNETIC ANOMALY

The UAV/drone used for this magnetometer survey was a DJI Inspire 2, equipped with a fluxgate magnetometer (shown at take-off in Fig. 10.15). The total take-off weight of the drone with the magnetometer system is ~3.75 kg. The theoretical maximum flight speed is 94 km h^{-1} As a safety measure the key system components are duplicated. Modification of the drone for this aerial magnetometer survey application primarily consist of holders for the magnetometer module, a modified chassis, and a sensor cable incorporated into the landing gear.

The drone and control systems carried to site are shown in Fig. 10.16. The drone is controlled by a native DJI interface with dual-band 2.400–2.483 GHz and 5.725–5.850 GHz communication. The flight parameters, setting of profile waypoints and measurement control takes place from the ground station via a tablet and remote controller. The magnetometer is a three-axis vector fluxgate sensor with flat ring core. The measurement range is +-75uT, nonlinearity is < 0.05%, with a noise level < 20 pT rms/√Hz per 1Hz. The three-component orthogonality after calibration is < 0.1°. Sensor location is determined by GPS and GLONASS positioning and altitude control with estimated accuracies of 1.5 m vertical and 3 m horizontal. Data sampling is at 62.5 or 250 samples/sec with the temperature of the sensor and unit and system information data recorded together with the magnetic field data.

The magnetometer has been designed specifically for UAV aerial magnetometry. It consists of a three-axis vector fluxgate magnetometer with flat-ring cores. The magnetometer is suspended on a 2.5 m long cable below the UAV. The control electronics of the magnetometer, GPS receiver, and power supply are fixed to the drone body. The complete magnetometer system, including the battery, weighs ~750 g. The magnetometer is independent of the drone and has its own power supply and is independent of GPS and GLONASS positioning. Data stored on the memory card for each measurement point at a frequency of 62.5 Hz are the three orthogonal components of the magnetic field, GPS position coordinates, altitude, temperature, and other system information.

Fig. 10.16. The complete mobile UAV system carried to site.

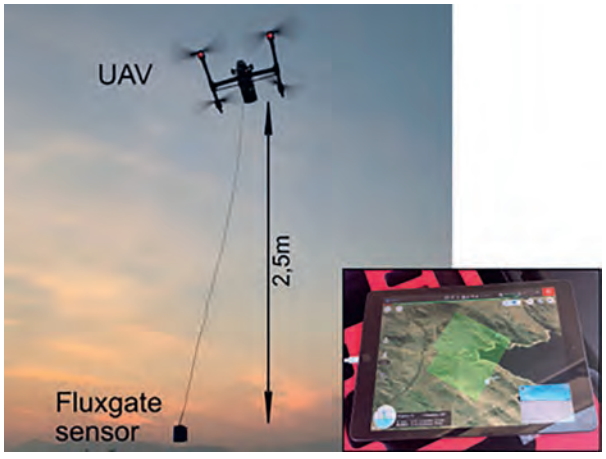

Fig. 10.15. UAV in flight with magnetometer sensor hanging down (left). UAV position during survey is streamed in real time to the ground station (right).

10.3.1 The UAV data acquisition

Two independent surveys were conducted at fixed altitude. Survey 1 (S1) at a mean altitude of 58 m above ground and the smaller Survey 2 (S2) at a mean altitude of 35 m above ground. The Jindabyne survey area has a topographic range of ~80 m. The ground station established in the north-east of the S1 area, near the topographic peak provided a clear view and visual contact with the drone at all times. The survey flight plan had been pre-designed and required only slightly modification for safety considerations after an on-site evaluation.

The drone was assembled on site and the magnetometer was connected. The transmitter was paired with the ground station before the magnetometer and drone were turned on and paired with the controller. The GPS satellite selection was made and the home point was saved. At the same time the magnetometer position was calibrated. The complete survey path with all way-points had been uploaded and stored in the drone's memory.

The magnetometer recording was started just before take-off and continued throughout the survey in autonomous mode.

The batteries were changed regularly during the survey as planned in the survey design and choice of ground station. The battery level and the individual cell voltages were monitored in real time during the entire survey both automatically by the drone and also by operator overview. Depending on the distance from the ground station and the estimated remaining available flight time, the drone regularly returned to the ground station where it landed for battery replacements, which was performed in about one minute. The drone then autonomously took off and flew to the position (both vertical and horizontal location) of the last magnetic measurement point to resume magnetic survey measurements. Neither the drone or the magnetometer needed to be turned off during the battery replacement, and the magnetometer data recording was not paused. Data acquired outside the measured profiles during battery replacement are removed from the measurement set in post-survey data processing.

Survey S1 (Fig. 10.17) is a grid of 43 parallel profiles with a spacing of 20 m and a total profile length of 43,974 m. The mean altitude is 58 m above ground. When planning the S1 profiles it was necessary to consider the slope to the north-east. The highest point in the survey area limits the lowest possible height for a fixed altitude survey (if a lower elevation had been required the survey could have been flown on a variable elevation drape surface). The point selected as the ground station was the highest point in the survey area that was suitably free of obstacles for take-off and landing.

The survey includes 86 turning points. The flight speed was set at 54 km/h. Take-off and landing were vertical. All other movements of the UAV over the surveyed area were at fixed altitude. Three battery replacements were required during the survey. These were performed at ends of profiles to both minimise distance to the ground station and reduce disruption of the data acquisition (for locations of the break points see Fig. 10.17). Survey area S2 (Fig. 10.18) is a subset of the S1 area flown with a different profile orientation and at a lower altitude (a mean clearance of 35 m above ground). The lower altitude was possible because of the gentle slopes of this area near the shore of the lake. This survey has 16 parallel profiles and 32 turning points, flown with a single battery set. The profile spacing of 20 m and flying speed of 54 km h^{-1} are the same as for the S1 survey. The total profile length is 11,057 m.

The three mappings of the magnetic field by the aeromagnetic and two drone surveys are shown in the TMI images of Fig. 10.19. The mean elevation of the aeromagnetic data within the study area (not published in the data but recovered by adding the radar altimeter measurements of ground clearance to the SRTM ground elevation) is 1,008 m; 28 m and 58 m higher than the two drone surveys. TMI data ranges for the three surveys are listed in Table 10.2. Over the main anomaly the higher and lower elevation drone surveys have increased data ranges of +50% and +130% compared to the aeromagnetic survey and the increases in amplitude are higher for the smaller southern anomaly that is poorly sampled by the aeromagnetic survey. The principal advantage of the magnetic field mapping from the drone surveys is the closer line spacing rather than the increase in amplitude due to their lower elevations.

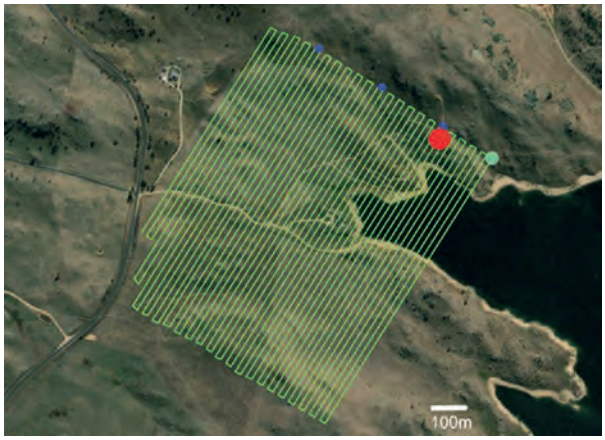

Fig. 10.17. Survey S1 flight lines. The red point is the ground station, the green point is the survey start location and the blue points mark survey breaks for battery replacement.

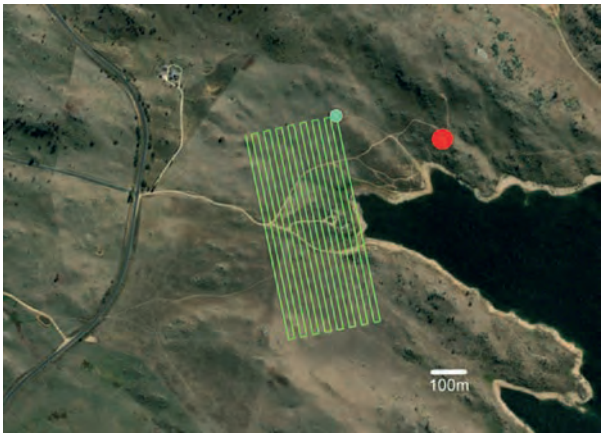

Fig. 10.18. Survey S2 flight lines. The red point is the ground station, the green point is the survey start location.

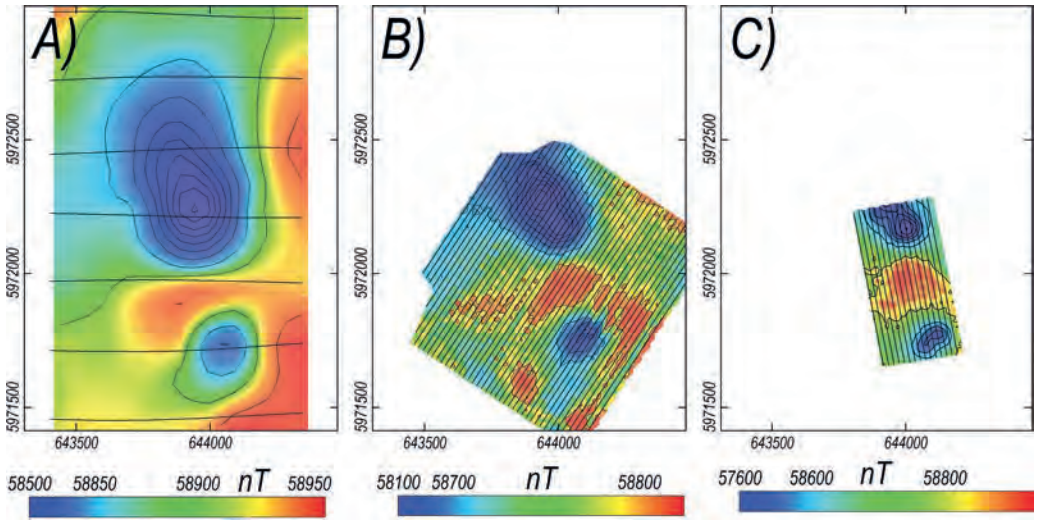

Fig. 10.19. TMI images: A) aeromagnetic survey, B) drone survey S1, C) drone survey S2.

Table 10.2. Magnetic survey data ranges.

Anomaly	Aeromagnetic range (nT)	Survey S1 range (nT)	Survey S2 range (nT)
Main	470	710	1,100
Southern	190	260	640

10.3.2 Modelling of the UAV survey results

The UAV data was inverted using the same ModelVision software and methodology as was used for the aeromagnetic data inversions. Figure 10.20A shows TMI measured on the larger, higher elevation S1 UAV survey over the main aeromagnetic anomaly. The corresponding field computed from a polygonal pipe model derived from inversion of this data is shown in Fig. 10.20B. The trough of the anomaly is the combination of a dominant minimum to the north-west and a secondary minimum to the south-east. These may be expressions of a single complex magnetisation or two smaller, close magnetisations producing anomalies with extreme overlap. A ground survey would be required to reliably discriminate between these model options. We choose to model the anomaly as due to a single complex body. Inversion of this model permits horizontal movement of the individual vertices as well as changes to the elevation of the top surface, magnetisation intensity and direction, depth extent and plunge. We also inverted the anomaly with models of simpler geometry. Each model occupies almost

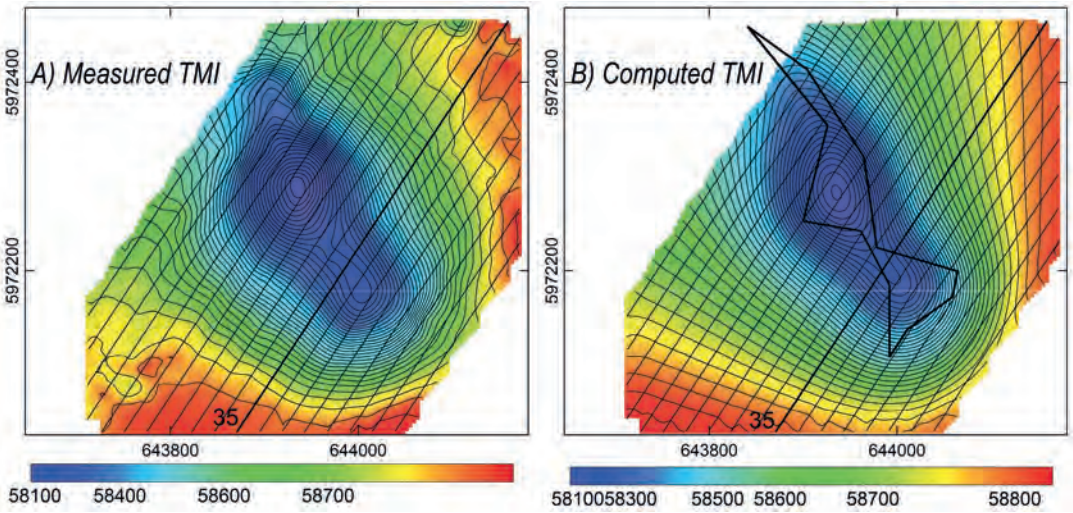

Fig. 10.20. S1 survey Larger Anomaly TMI: A) measured, B) model computed.

the same space (Fig. 10.21) and all have similar magnetisation directions (Table 10.1). All models acceptably match the data but the additional complexity of the polygonal pipe model provides the best fit with a model that has two lobes, one over each of the trough minima. Figure 10.21 shows a section through the model along one of the central flightlines and a perspective view of the overlap of the alternative models.

Figure 10.22A shows an equivalent image of TMI over the smaller southern anomaly measured from the lower elevation S2 UAV survey and Fig. 10.22B shows the field forward computed from a polygonal pipe inversion mode derived from inversion of that data. This anomaly is more compact but of equivalent complexity to the S1 Larger Anomaly. The polygonal pipe inversion of this anomaly also develops a model with two nodes (Fig. 10.22B). A flightline traverse through this and the alternative models is shown in Fig. 10.23A. The different models again occupy almost the same space (Fig. 10.23B) and have similar magnetisation directions (Table 10.1).

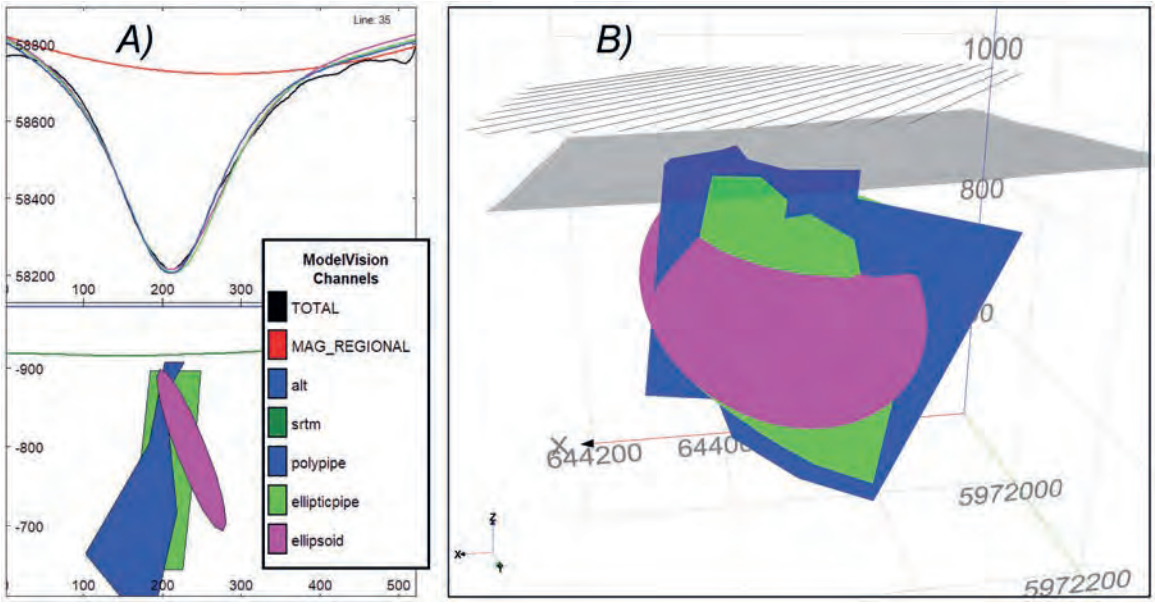

Fig. 10.21. S1 survey Larger Anomaly: A) central flightline section, B) model perspective view.

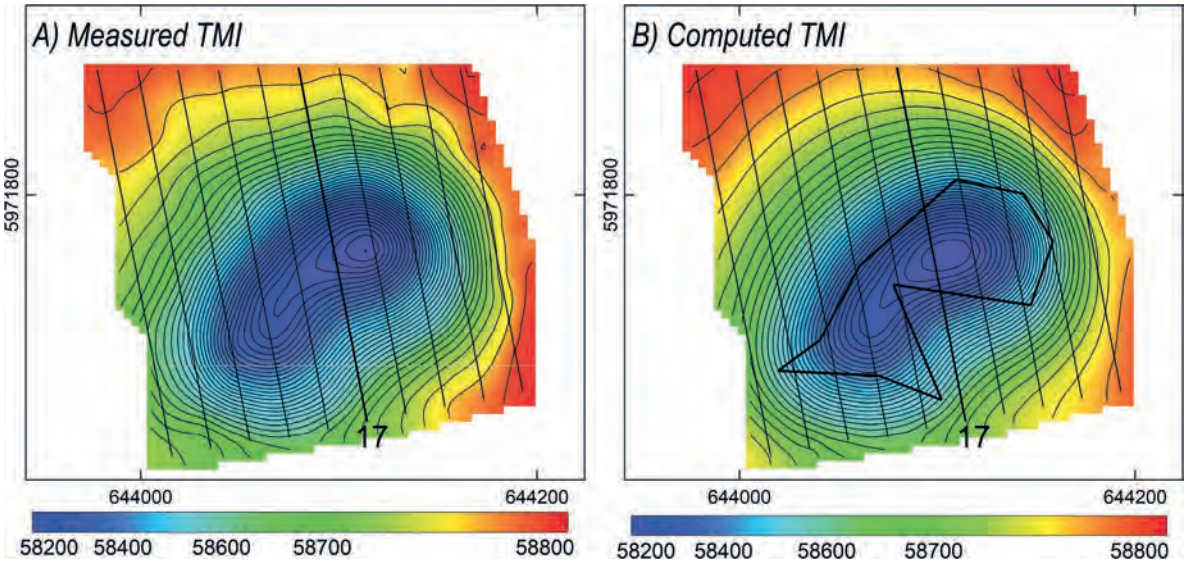

Fig. 10.22. S2 survey Smaller Anomaly TMI: A) measured, B) model computed.

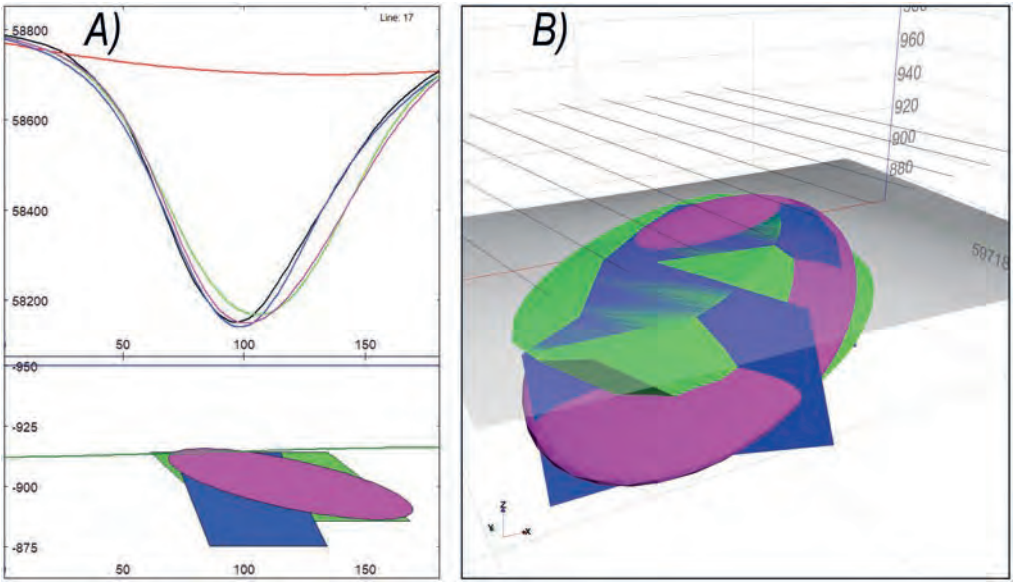

Fig. 10.23. S2 survey Smaller Anomaly: A) central flightline section, B) model perspective view.

10.4 ESTIMATION OF MAGNETISATION DIRECTION FROM THE AEROMAGNETIC AND UAV DATA

The model magnetisation directions listed in Table 10.1 are plotted on a stereonet in Fig. 10.24. Four datasets were inverted: the main anomaly measured on the aeromagnetic survey and on the higher UAV survey, and the southern anomaly measured on both UAV surveys. The southern anomaly is insufficiently sampled on the aeromagnetic survey for meaningful modelling, and the main anomaly was only partially covered on the lower UAV survey. The difference between the mean directions of the three models from each of the two surveys of the main anomaly is 12° and the difference between the mean directions of the three models from each of the two surveys of the main anomaly is 11°. The difference between the mean direction of the six inversions of the main anomaly data (blue symbols in Fig. 10.24) and of the six inversions of the southern anomaly data (red symbols in Fig. 10.24) is 12°. Visual inspection of the directions in Fig. 10.24 suggests that the directions for the two anomalies (the red and blue symbols) may belong to two slightly different populations and the difference between them would be consistent with secular variation between slightly different emplacement and (rapid) cooling ages for the two bodies.

In this study the estimated magnetisation direction for the main anomaly has not changed appreciably from analysis of the aeromagnetic data to analysis of magnetisation data from the UAV survey, but the UAV survey has substantially increased confidence in this direction. The UAV survey has also provided a magnetisation direction estimate for the southern anomaly, that was insufficiently sampled by the aeromagnetic survey to justify estimation of its magnetisation direction. These results from the surveys at Jindabyne are consistent with the synthetic modelling results presented earlier.

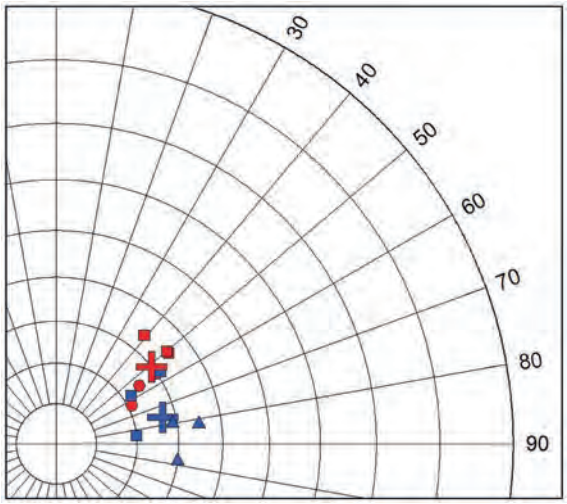

Fig. 10.24. Model magnetisation directions, blue – main anomaly, red – southern anomaly, triangles – aeromagnetic survey, squares – higher UAV survey, circles – lower UAV survey.

ACKNOWLEDGEMENTS

Marian Takáč and Gunther Kletetschka were partially supported from the Czech Science Foundation 20–08294S, and MEYS, LTAUSA 19141.

REFERENCES

Beiki M, Clark DA, Austin JR, Foss CA (2012) Estimating source location using normalized magnetic source strength calculated from magnetic gradient tensor data. *Geophysics* **77**, J23–J37. doi:10.1190/geo2011-0437.1

Foster DA, Gray DR (2000) The structure and evolution of the Lachlan Fold Belt (Orogen) of eastern Australia. *Annual Review of Earth and Planetary Sciences* **28**, 47–80. doi:10.1146/annurev.earth.28.1.47

Helbig K (1963) Some integrals of magnetic anomalies and their relation to the parameters of the disturbing body. *Zeitschrift für Geophysik* **29**, 83–96.

Lewis PC, Glen RA (1995) 'Bega-Mallacoota 1:250 000 Geological Sheet SJ155–4 SJ155–8. Second edition.' Geological Survey of New South Wales, Sydney.

Lewis PC, Glen RA, Pratt GW, Clarke I (1994) 'Bega-Mallacoota 1:250 000 Geological Sheet SJ155–4 SJ155–8: Explanatory Notes.' Geological Survey of New South Wales, Sydney.

Li X (2006) Understanding 3D analytic signal amplitude. *Geophysics* **71**, L13–L16. doi:10.1190/1.2184367

Medeiros WE, Silva JBC (1995) Simultaneous estimation of total magnetization direction and 3-D spatial orientation. *Geophysics* **60**, 1365–1377. doi:10.1190/1.1443872

Reid AB (1980) Aeromagnetic survey design. *Geophysics* **45**, 973–976. doi:10.1190/1.1441102

Roest W, Pilkington M (1993) Identifying remanent magnetization effects in magnetic data. *Geophysics* **58**, 653–659. doi:10.1190/1.1443449

Wijns C, Perez C, Kowlczyk P (2005) Thetamap: edge detection in magnetic data. *Geophysics* **70**, L39–L43. doi:10.1190/1.1988184

Zietz I, Andreasen GE (1967) Remanent magnetization and aeromagnetic interpretation. *Mining Geophysics* **2**, 569–590.